11th International Symposium on Turbulence and Shear Flow Phenomena (TSFP11)
Southampton, UK, July 30 to August 2, 2019

FLOW SEPARATION CONTROL BY SPANWISE ALTERNATING WALL ACTUATION

Weidan Ni

National Key Laboratory of Science and
Technology on Aero-Engine Aero-Thermodynamics
School of Energy and Power Engineering
Beihang University, Beijing, 100191, China
Scientific Computing Department
Science & Technology Facilities Council (STFC)
Daresbury Laboratory, Warrington, WA4 4AD, UK
weidan.ni@buaa.edu.cn

Jian Fang

Scientific Computing Department
Science & Technology Facilities Council (STFC)
Daresbury Laboratory, Warrington, WA4 4AD, UK
jian.fang@stfc.ac.uk

Charles Moulinec

Scientific Computing Department
Science & Technology Facilities Council (STFC)
Daresbury Laboratory, Warrington, WA4 4AD, UK
charles.moulinec@stfc.ac.uk

David R. Emerson

Scientific Computing Department
Science & Technology Facilities Council (STFC)
Daresbury Laboratory, Warrington, WA4 4AD, UK
mailto:charles.moulinec@stfc.ac.uk
david.emerson@stfc.ac.uk

Yufeng Yao

Faculty of Environment and Technology
Department of Engineering Design and
Mathematics, University of the West of England
Bristol, BS16 1QY, UK
Yufeng.Yao@uwe.ac.uk

Lipeng Lu

National Key Laboratory of Science and
Technology on Aero-Engine Aero-Thermodynamics
School of Energy and Power Engineering
Beihang University, Beijing, 100191, China
lulp@buaa.edu.cn

ABSTRACT

An implicit large-eddy simulation (ILES) is carried out to study the turbulent boundary layer separation from a backward-facing rounded ramp with active wall actuation control. This method, called spanwise alternating distributed strips (SADS) control, is imposed onto the flat plate surface upstream of the rounded ramp by alternatively applying out-of-phase control (OPC) and in-phase control (IPC) to the wall-normal velocity component in the lateral direction. As a result, the local turbulence is alternatively suppressed by the OPC strips and enhanced by the IPC strips, leading to the creation of a vertical shear layer, which is responsible for the presence of large-scale streamwise vortices (LSSVs). These LSSVs, thought to be similar to Prandtl's second kind of secondary flow, can be further sustained by the SADS control, exerting a predominant influence on the suppression of the flow separation. The interaction between the LSSVs and the downstream recirculation zone and free shear layer is studied by examining flow statistics, including skin-friction and pressure coefficients, skin friction streamlines, mean streamwise velocity, turbulent kinetic energy and Reynolds stresses. It is found that in comparison with the non-controlled case, the flow separation is delayed, the reattachment point is shifted upstream, and the size of the mean recirculation zone is therefore reduced. A better performance with regards to the separation point is achieved by the case with L_{IPC}^{+}=387 (Case WE). The case with L_{IPC}^{+}=155 (Case W5) behaves better in terms of the reattachment point and the length of the separated zone. The analyses show that the delay of the flow separation is attributed to the activation of the near-wall turbulence by the IPC strips and the improvement of the reattachment location is mainly due to the LSSVs.

INTRODUCTION

Flow separation control is probably the oldest and yet most crucial element in economic sense among all the existing flow control methods since many negative influences on the performance of vehicles and devices are induced by the flow separation, including drag increase, flow blockage and instability. An effective strategy of suppressing flow separation is to energise the near-wall fluids by enhancing the momentum transport across the boundary layer via the introduction of large-scale streamwise vortices (LSSVs) inside the boundary layer. The aim of the present research is to explore the feasibility of controlling flow separation by inducing LSSVs using a kind of small-scale control method, namely spanwise alternating distributed strips (SADS) control.

METHODOLOGY

The three-dimensional (3-D) unsteady compressible Navier-Stokes equations are solved using implicit large-eddy simulation (ILES). The ILES of the flow past a backward-facing rounded ramp is first performed as the baseline case (Case NC). The geometry of the rounded ramp corresponds to the configuration in the large-eddy simulation (LES) study of Lardeau and Leschziner (2011) and Bentaleb et al. (2012). The domain spans from x = -30.0 to 25.0 in the streamwise direction. A rounded ramp step of height H is attached to the flat plate at x = 0.0. The flow conditions are set as: Re = 7,106 (based on the freestream velocity and the height of the ramp H) and M = 0.2. The size of the computational domain in the streamwise and spanwise directions is $L_x \times L_z$ = 55×5 and for the wall-normal direction, L_y changes from 8 (upstream of the ramp) to 9 (downstream of the ramp). The computational domain is discretised by a mesh with $1290 \times 200 \times 300$ nodes. The results are validated by comparing the baseline with the incompressible DNS database of Schlatter and Örlü (2010) and Jeménez et al. (2010). The sketch of the control method is presented in Figure 2a. The SADS control is imposed onto the flat plate surface upstream of the ramp from x_{start} = -10.0 to x_{end} = 0.0 by alternatively applying out-of-phase control (OPC) and in-phase control (IPC) in the spanwise direction. OPC and IPC are given as $v_{wall}(x,z) = \mp Av(x, y_{dtc}, z)$, respectively. $v_{wall}(x,z)$ is the wall-normal velocity at the wall. The coefficients A is to control the amplitude of the wall velocity, which are set to 0.5. y_{dtc} is the detected position set to a fixed value of y coordinate at the 15th mesh node away from wall. The corresponding non-dimensional value y^+_{dtc} ranges from 12 ($x = x_{start}$) to 15 ($x = x_{end}$), based on the wall values of the baseline case. Two controlled cases (Cases W5 and WE) with different IPC/OPC widths are studied, and the widths of IPC strips are summarised in Table 1.

REUSULTS AND DISCUSSION

The turbulence coherent structures above the backward-facing rounded ramp and its neighbouring upstream and downstream regions, identified by the iso-surfaces of the Q criterion and coloured by the instantaneous streamwise velocity u, are presented in Figure 1 for all cases. Compared with the baseline case, the turbulence coherent structures of cases with SADS are alternatively redistributed over the controlled region. In general, these turbulence coherent structures are enhanced above the IPC strips, whereas above the OPC strips, a suppression of the coherent structures can be observed. The flow field above the controlled zone demonstrates a phase-locked reorganisation in correspondence with the topography configuration of the SADS distribution. The alternatively modified coherent structures above OPC/IPC strips indicate the evidence of suppression/enhancement of local turbulence. Furthermore, the alternating distributed suppressed and enhanced turbulence coherent structures can extend to the downstream of the controlled area, which is more distinct in the case with wider width of IPC strips (Case WE), as illustrated in Figure 1c.

The mean statistics are analysed in detail in the following. The streamwise variation of the skin friction coefficient and pressure coefficient are firstly dealt with based on their respective spanwise- and time-averaged statistics and presented in Figure 3. The mean skin friction coefficient C_f and pressure coefficient C_p are defined as,

$$C_f(x) = \frac{\mu_w \partial \langle \overline{u} \rangle_z / \partial y|_w}{\frac{1}{2}\rho_\infty u_\infty^2} \tag{1}$$

and

$$C_p(x) = \frac{\langle \overline{P} \rangle_z - P_\infty}{\frac{1}{2}\rho_\infty u_\infty^2} \tag{2}$$

For the controlled cases, the SADS control causes the increase of the skin friction upstream of the rounded ramp, due to the intense activation of turbulence locally by the IPC strip. Case WE shows a larger skin friction upstream of the ramp and this can be attributed to the wider width of the IPC strip. After reaching the ramp, the flow decelerates because of the adverse pressure gradient and separation occurs. For the baseline case, the time-averaged separation occurs at x = 0.79. The separation and reattachment locations as well as the length of the separated zone for all the cases studied in the present research are summarised in Table 2. It can be seen from Figure 3a and Table 2 that a better performance with regards to the separation position is obtained by Case WE due to wider width of the IPC strip. We suggest that the enhanced turbulence above the IPC strips goes downstream and then increases the momentum transport of the corresponding downstream region, further leading to the delay of the separation. Further downstream of the ramp, the flow reattaches at x = 5.03 for the baseline case. However, after SADS control is imposed, the flow shows a better performance regarding the reattachment location and Case W5 behaves better compared with Case WE. Besides, the shorter length of the separated zone is also achieved by Case W5 as shown in Table 2. Since much lower skin friction is induced by Case W5 upstream of the ramp, the controlling parameters of Case W5 are preferable to suppress the flow separation. It can be seen from Figure 3b that there exists a plateau within the separated near-wall region for the baseline case whilst this plateau is lifted up after imposing SADS control, especially for Case WE. This indicates that the control method adopted in the present study increases the pressure in the recirculation zone and plays a positive role in reducing pressure drag.

The distribution of the skin friction coefficient and the skin friction streamlines for all the cases calculated by the time-averaged statistics are plotted in Figure 4. For the controlled cases, a distinct node around the separation line can be observed downstream of the IPC strips whereas a saddle is seen between the neighbouring nodes downstream of the OPC strips as illustrated in Figure 4b and c. The flow topology of the controlled cases is reorganised by alternatively distributed OPC and IPC strips. It is shown in Figure 4a that five nodes around the reattachment line can be recognized in Case NC whereas the number of the nodes in the corresponding region is reduced to three for both controlled cases. It indicates that the spanwise spacing of the neighbouring nodes is increased by SADS control, suggesting larger flow structures are dominating the flow reattachment. This should be the main mechanism of the control method in improving the performance of flow reattachment.

The profiles of the time and spanwise-averaged streamwise velocity selected from nine representative streamwise positions are presented in Figure 5. It can be seen from Figure 5 that Case W5 shows a more effective influence on the second half of the recirculation zone and Case WE exhibits a better control effect on the first half of the separated flow. As indicated in Figure 5b, the near-wall flow is accelerated under the inflection point of the velocity profile in the recirculation zone after imposing SADS control whereas the velocity in the outer part of the free shear layer slightly decreases compared with Case NC. This indicates that there exists large-scale structures in the controlled case, which enhances the momentum transport between the main flow and the separated flow since the inflection point of the streamwise velocity profile can be regarded as the edge of the recirculation zone. Therefore, the separated flow in the controlled case has a great potential to realise the flow recovery. It can also be observed that the inflection points seen in Case

WE shift towards the wall compared with those from the baseline case, demonstrating that the flow separation is effectively suppressed by SADS control.

The mean streamwise velocity fields of all the cases at x = 0.8, 3.0 and 5.0 are compared in Figure 6 to show the spanwise variation of the mean streamwise velocity. As observed in Figure 6b and 6c, around the separation point of Case NC, the near-wall velocity increases above the wall downstream of IPC region, whereas large-scale low-speed regions are induced above the wall downstream of OPC strips. The accelerated fluid above the wall downstream of IPC regions play a critical role in delaying the flow separation as the ability of the fluid to resist flow separation is enhanced. Therefore, a reasonable interpretation is that the wider the IPC strips are, the better the delay of the flow separation works. This is also consistent with the mean separation locations summarised in Table 2, showing that Case WE exhibits better separation delay. It can be seen from Figure 6i that the height of the separation bubble is reduced above the wall downstream of IPC strips, whereas in the limited regions over the wall downstream of OPC strips, the recirculation zone enlarges in the wall-normal direction. This suggests that the control method adopted in the present research takes a prominent role in suppressing flow separation. For Case W5 in the corresponding streamwise position as indicated in Figure 6h, the positive effects exerted on the flow field extend to the neighbouring downstream of OPC strips, especially for those located at the left-hand side of downstream of IPC strips. This differs from the approximate phase-locked variation of the mean streamwise velocity imposed by Case WE. In the reattachment region of Cases W5 and WE, as indicated in Figure 6h and 6i, spanwise alternating distributed low- and high-velocity regions can be observed. Therefore, the large-scale structures are induced by the alternating distributed OPC and IPC strips upstream of the rounded ramp, and they can be sustained downstream of the rounded ramp and interact with the separation bubble and the reattachment flow.

The distribution of $TKE|_t$ and $RSS|_t$ based on the time-averaged statistics as well as mean velocity vector $(\overline{w}, \overline{v})$ at x = 0.8, 3.0 and 5.0 for Cases NC, W5, and WE are presented in Figure 7 and Figure 8, respectively, in order to further study the properties of the LSSVs and the momentum transport. The definition of $TKE|_t$ and $RSS|_t$ is given as

$$TKE|_t = \frac{1}{2}\overline{u'_k u'_k} \quad (k = 1, 2, 3) \tag{3}$$

and

$$RSS|_t = \overline{u'v'} \tag{4}$$

$TKE|_t$ and $RSS|_t$ are normalised by the square of the reference velocity u_{ref}^2 in Eqs. (3) and (4). " $|_t$" expresses that the fluctuation is calculated by subtracting the time-averaged velocity from the instantaneous one. A similar distribution of $TKE|_t$ and $RSS|_t$ for the controlled cases can be observed around the separation location, as illustrated in the first rows of Figure 7 and Figure 8. As the near-wall turbulence is enhanced downstream of IPC strips, the separation locations of Cases W5 and WE are delayed due to their ability to resist flow separation improved. The control effect with regards to the separation delay is proportional to the width of the IPC strips upstream. This is consistent with the mean separation locations of all the cases summarised in Table 2. It can be seen from Figure 7d and Figure 8d that most of TKE and RSS is confined in the free shear-layer for the baseline case after the flow reaches the separated region. However, for Cases W5 and WE, the $TKE|_t$/ $RSS|_t$ in the free shear-layer are redistributed by the sweep and ejection motions. The sweep motions can be observed downstream of IPC as illustrated in Figure 7e and f (Figure 8e and f). They bring the high momentum fluid from the free shear-layer into the separation bubble, leading to the high $TKE|_t$ and $RSS|_t$ obtained in the near-wall region. The enhanced turbulent momentum transport results in the decrease of the height of the separation bubble as shown by the solid black lines in Figure 7e and f (Figure 8e and f). It is worth mentioning that the reduction in the height of the separated region is not limited to the regions downstream of the strips, especially for Case W5. It indicates that Case W5 exhibits a better control effect with a narrower width of upstream IPC strips. On the other hand, the ejection motions take the low momentum fluid from the inner part to the outer region of the separation bubble, enhancing the mixing procedure between the recirculation region and the free shear-layer. Compared with Case WE, the $TKE|_t$ and $RSS|_t$ in the free shear-layer downstream of OPC strips are enhanced by Case W5. As reported by Le et al. (1997) there exists an oscillatory large-scale roll-up of the shear-layer extending to the reattachment region in the turbulent flow over a backward-facing step, leading to the motion of the reattachment location(s) in the streamwise direction. Therefore, the large-scale structures generated by SADS control interact with the large-scale vortices in the free shear-layer, leading to the reattachment locations being shifted upstream. Since the large-scale motions generated by Case W5 have a relatively stronger impact on the distribution of $TKE|_t$ and $RSS|_t$ in the free shear-layer, the best control effect with regards to the reattachment location is achieved by Case W5. The counter-rotating LSSVs can be clearly seen in the reattachment regions, as observed in Figure 7h and i (Figure 8h and i). The spanwise distribution of alternating high-low $TKE|_t$ and $RSS|_t$ streaks corresponds to the low-high mean streamwise velocity streaks in Figure 6h and i, exhibiting that the ejection and sweep motions are the major events related to the momentum transports. The penetration depth of the large-scale motions displays the same order of magnitude as the local turbulent boundary-layer thickness.

CONCLUSION

- With spanwise alternating distributed OPC/IPC strips, the distribution of the flow field is modified in the spanwise direction.
- The analyses confirm that the LSSVs can be generated by SADS control. They have an effective interaction with the downstream free shear layer and then reduce the size of the separated regions. The flow in the separated region presents a strong 3-D characteristic, and the overall reduction of the mean separation zone is achieved due to the delay of the separation line and the forward shift of the reattachment line.
- The delay of the separation point is attributed to the local activation of the near-wall turbulence by IPC strips and the performance improvement with regards to the reattachment location is mainly due to the LSSVs.

REFERENCES

Bentaleb, Y., Lardeau, S. and Leschziner, M.A., 2012, "Large-eddy simulation of turbulent boundary layer separation from a rounded step", *Journal of Turbulence*, Vol. 13, No. 4.

Jiménez, J., Hoyas, S., Simens, M.P. and Mizuno, Y., 2010, "Turbulent boundary layers and channels at moderate Reynolds numbers", *Journal of Fluid Mechanics*, Vol. 657, pp. 335-360.

Lardeau, S. and Leschziner, M.A., 2011, "The interaction of round synthetic jets with a turbulent boundary layer separating from a rounded ramp", *Journal of Fluid Mechanics*, Vol. 683, pp. 172-211.

Le, H., Moin, P. and Kim, J., 1997, "Direct numerical simulation of turbulent flow over a backward-facing step," *Journal of Fluid Mechanisms*, Vol. 330, pp. 349-374.

Schlatter, P. and Örlü, R., 2010, "Assessment of direct numerical simulation data of turbulent boundary layers", *Journal of Fluid Mechanics*, Vol. 659, pp. 116-126.

Table 1 Summary of the ILES cases in the present study.

Case	L_{IPC}	L^+_{IPC} [a]
NC	Baseline case without control	
W5	$0.5H$	155
WE	$1.25H$	387

[a] L^+_{IPC} refers to L_{IPC} normalised by the wall viscous length scale of Case NC at x_{start}.

Table 2 Summary of the time- and spanwise-averaged separation and reattachment locations as well as the length of the separated zone of all the cases

Case	Separation location	Reattachment location	Length of the separated zone
NC	0.79	5.03	4.24
W5	0.84	4.72	3.88
WE	0.92	4.83	3.91

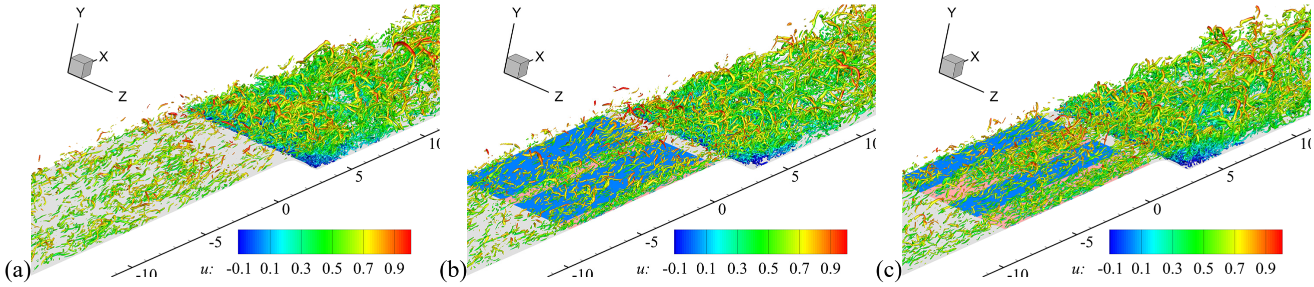

Figure 1. Turbulence coherent structures visualised with iso-surfaces of Q criterion and colored by instantaneous streamwise velocity u. The strips colored by blue and red on the wall upstream of the rounded ramp represent OPC and IPC regions, respectively. (a) Case NC; (b) Case W5; (c) Case WE.

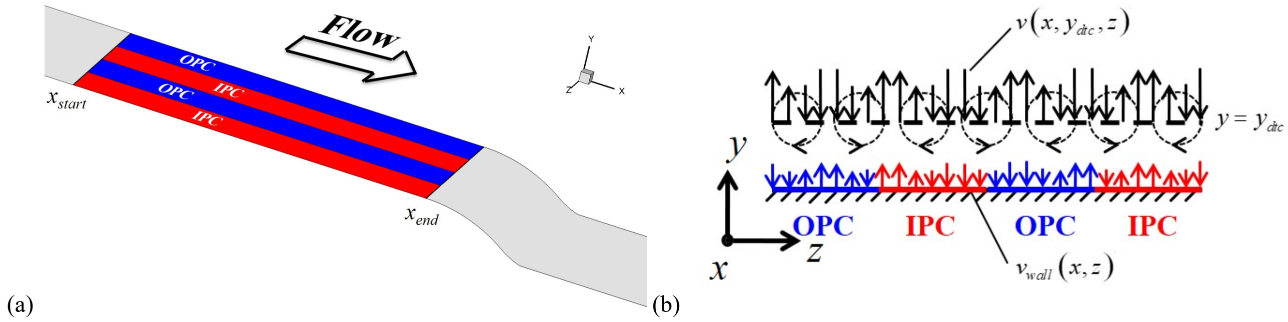

Figure 2. Sketch of the topography configuration with alternatively imposed out-of-phase control (OPC, blue) and in-phase control (IPC, red) strips (a) and principle of the control method (b).

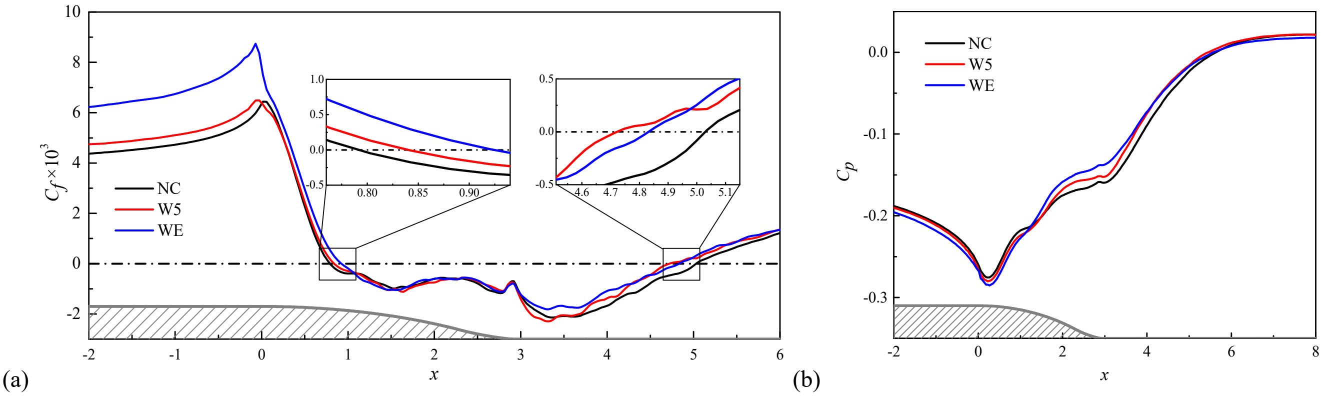

Figure 3. Skin friction coefficient C_f (a) and pressure coefficient C_p (b) based on spanwise- and time-averaged flow field. The grey line at the bottom of the figure and its underneath filled area represent the shape of the geometry adopted in the present study.

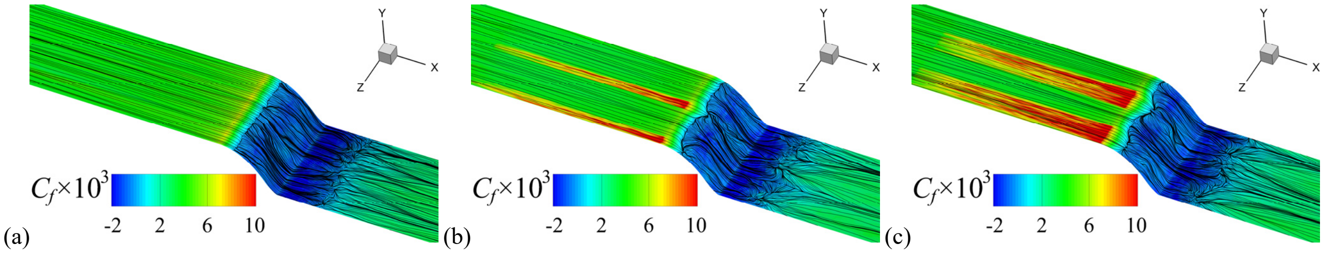

Figure 4. Time-averaged skin friction coefficient and skin friction lines. (a) Case NC; (b) Case W5; (c) Case WE.

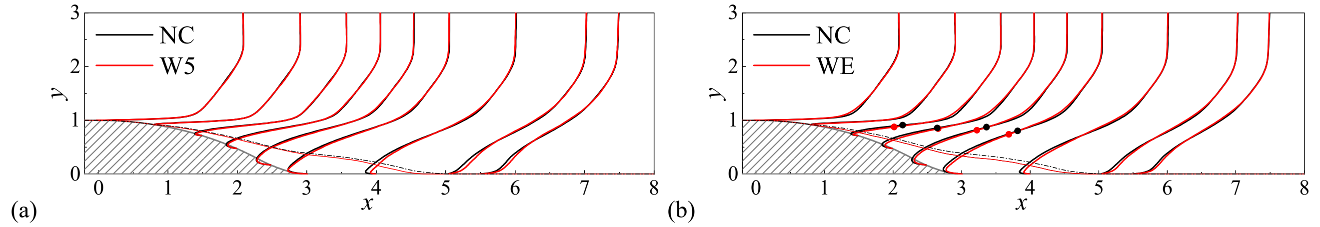

Figure 5. Profiles of the time- and spanwise-averaged streamwise velocity at x = 0.0, 0.8, 1.5, 2.0, 2.5, 3.0, 4.0, 5.0, 5.5. The zero-streamwise-velocity locations are represented by dashed-dotted black line and solid red lines for the baseline case and the controlled cases, respectively. The black and red solid circles in (b) represent the inflection points of the mean streamwise velocity profiles for the baseline case and the controlled case, respectively.

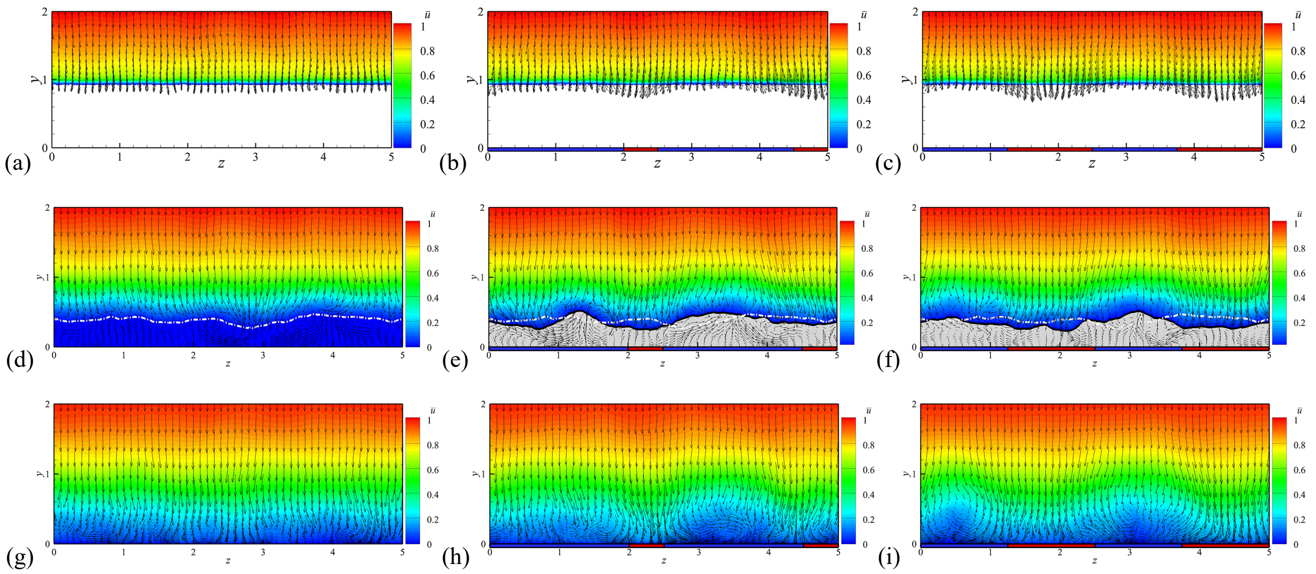

Figure 6. Time-averaged streamwise velocity as well as time-averaged velocity vector $(\overline{w}, \overline{v})$ of Cases NC, W5, and WE from the left-hand side to the right-hand side, respectively. The results come from x = 0.8, 3.0 and 5.0 from top to bottom. The zero-streamwise-velocity location of Case NC is shown as dashed-dotted white line in (d), (e) and (f) while those of Cases W5 and WE are shown as solid black lines. The areas filled with grey in (e) and (f) represent the separated regions with SADS control. The blue and red strips with black borders plotted under the z-coordinate axis represent the corresponding regions downstream of the flat plate surface controlled by the OPC and IPC strips, respectively.

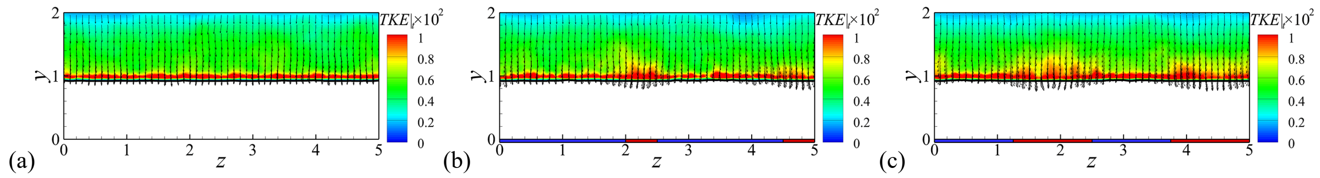

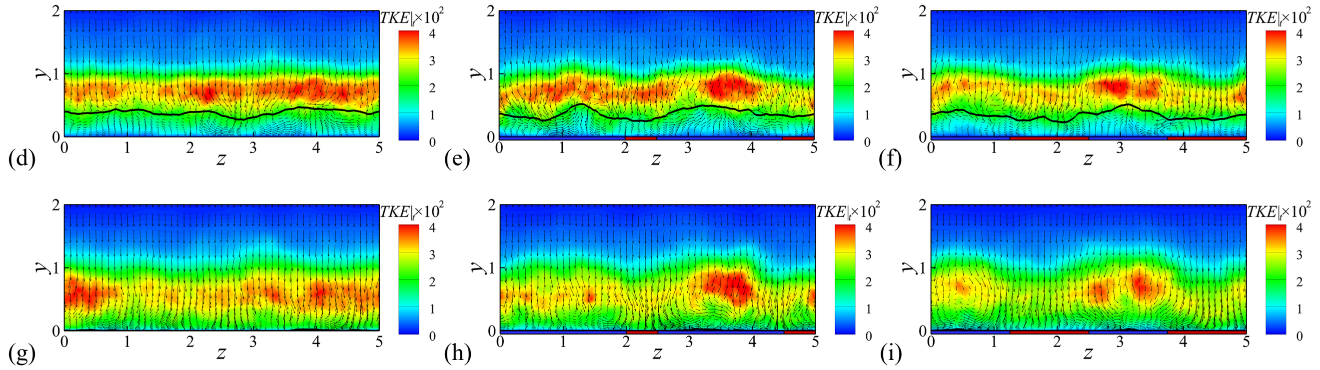

Figure 7. $TKE|_t$ as well as mean velocity vector $(\bar{w}, \bar{v})$ of Cases NC, W5, and WE from the left-hand side to the right-hand side, respectively, calculated by time-averaged statistics. The results come from x = 0.8, 3.0, and 5.0 from top to bottom. The zero-streamwise-velocity locations are shown as solid black lines for Cases NC, W5, and WE.

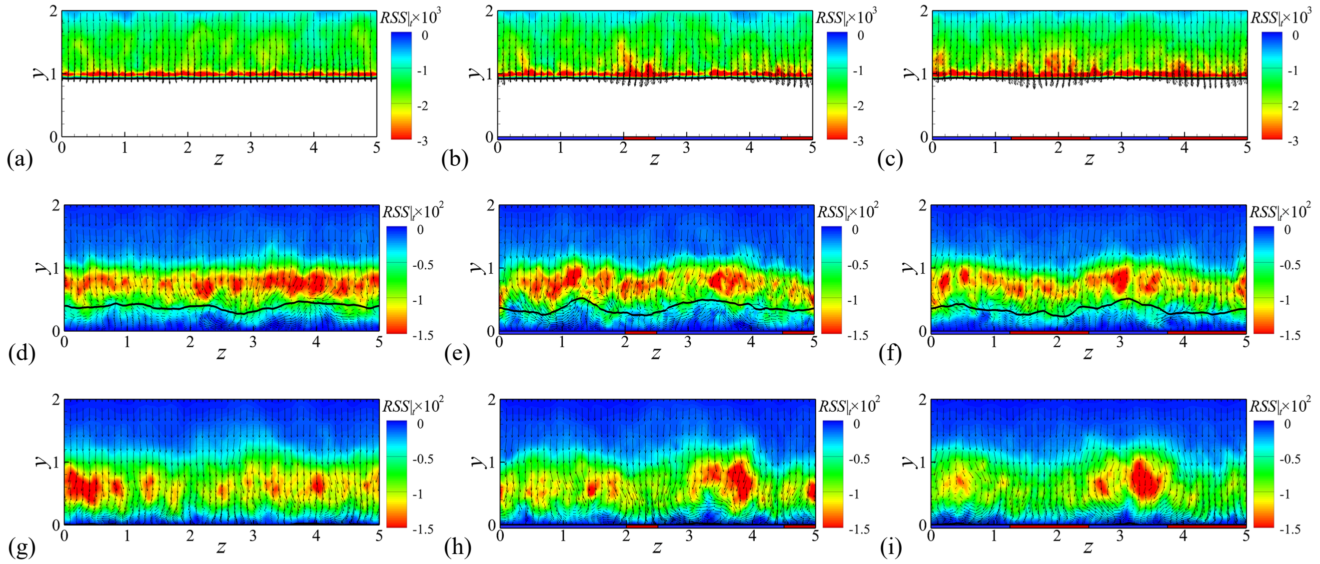

Figure 8. $RSS|_t$ as well as mean velocity vector $(\bar{w}, \bar{v})$ of Cases NC, W5, and WE from the left-hand side to the right-hand side, respectively, calculated by time-averaged statistics. The results come from x = 0.8, 3.0, and 5.0 from top to bottom. The zero-streamwise-velocity locations are shown as solid black lines for Cases NC, W5, and WE.